Stray light modeling of the James Webb Space Telescope (JWST) Integrated Science Instrument Module (ISIM)

Scott O. Rohrbach[*a], Ryan G. Irvin[b], Lenward T. Seals[a], Dennis L. Skelton[c]

[a]NASA Goddard Space Flight Center, 8800 Greenbelt Rd., Greenbelt, MD 20771
[b]Photon Engineering LLC, 310 S Williams Blvd. #222, Tucson, AZ 85711
[c]Sigma Space Corporation, 4600 Forbes Boulevard, Lanham, MD 20706

ABSTRACT

This paper describes an integrated stray light model of each Science Instrument (SI) in the Integrated Science Instrument Module (ISIM) of the James Webb Space Telescope (JWST) and the Optical Telescope Element Simulator (OSIM), the light source used to characterize the performance of ISIM in cryogenic-vacuum tests at the Goddard Space Flight Center (GSFC). We present three cases where this stray light model was integral to solving questions that arose during the testing campaign − 1) ghosting and coherent diffraction from hardware surfaces in the Near Infrared Imager and Slitless Spectrograph (NIRISS) GR700XD grism mode, 2) ghost spots in the Near Infrared Camera (NIRCam) GRISM modes, and 3) scattering from knife edges of the NIRCam focal plane array masks.

Keywords: JWST, ISIM, stray light, scattering, ghosting

1. INTRODUCTION

The Integrated Science Instrument Module (ISIM) of the James Webb Space Telescope (JWST) is comprised of four Science Instruments (SIs), the Fine Guidance Sensor (FGS), and the ISIM Structure, to which each of the instruments is mounted. Various levels of stray light modeling and tests of each instrument were performed prior to delivery to the Goddard Space Flight Center (GSFC), but it was determined that a single Observatory-level model, including all instruments and the ISIM Structure, was required to properly assess all of the specular, scattered, and thermal self-emission paths that could impact the performance of the Observatory. Therefore, a single, integrated model that includes ISIM, the Optical Telescope Element (OTE), and associated spacecraft hardware, including the large sun shield was built using the delivered optical models (CODE V and ZEMAX), CAD packages, thermal models, and reported surface coating and scatter property data. This integrated optomechanical model was constructed in the FRED Optical Engineering Software (FRED). The model is configurable between a flight Observatory system, the NASA GSFC cryogenic-vacuum test chamber setup, and two different representations of the NASA Johnson Spec Center (JSC) cryogenic vacuum "Chamber A" that support the OGSE2 and OTE + ISIM (OTIS) tests.

A simple outline of how each subsystem of the model was constructed includes:

1. (For optical subsystems) Import the optical prescription from CODE V or ZEMAX into FRED.

2. Validate the imported system by ray tracing identical chief rays in FRED and CODE V or ZEMAX models. Agreement between the optical models was achieved when the ray intercept differences at the focal planes were less than 30 nm.

3. In FRED, reconstruct the mechanical elements found in the CAD and/or thermal models by using a combination of native FRED constructs, imported Non-Uniform Rational B-spline (NURB) surfaces from CAD, or imported OBJ or STL geometry representations (approximations of native CAD designs using a tessellation of triangular surfaces). The mechanical elements reconstructed with the highest fidelity are found along the nominal optical paths, while elements away from the optical path have increasingly simplified representations. Due to the scale of JWST and its associated testbeds, faithful representation of all mechanical components by direct import of CAD hardware into FRED was both impractical and intractable. Since CAD models typically reflect the room temperature dimensions of the subsystem in question, the FRED subassemblies also need to be scaled to

---

[*] scott.rohrbach@nasa.gov, phone 1 301 286-3197

operational temperature, e.g.., the Mid-Infrared Instrument (MIRI) operates at 7K, the other SIs operate at ~37K, and the Optical Telescope Element Simulator light source (OSIM) operates at 100K.

4. In order to duplicate the hardware tests in the FRED model, the software model was automated, by use of the BASIC scripting language in FRED, to replicate the motions of various components in the systems (ex. mirror pointing of the OSIM, rotations of the science instruments (SIs) filter and pupil mechanisms, focusing of the SIs, steering of the autocollimating flats of the JSC tests, etc.). The scripts, embedded into the FRED model and called as libraries of functions, allow for extensible and reusable code that was repurposed for each of the various hardware tests being modeled.

5. Apply the appropriate surface properties, and implement a set of configuration management scripts to ensure that surface properties are maintained in a known state.

2. MODEL OVERVIEW

The model consists of four main subsystems; the ISIM, the OTE, and the configuration in question (flight Observatory, ISIM cryogenic-vacuum (CV) test hardware, including the Space Environment Simulator (SES) at GSFC and the OSIM steerable/tunable light source, and the JSC "Chamber A" cryogenic vacuum chamber that supports the OGSE2 and OTIS tests. By activating select components of these subsystems, the model can be put into one of the four different configurations to support modeling for flight observatory, OSIM/ISIM, OGSE2 and OTIS. The complete Flight Observatory model is shown in Figure 1, while configurations for the ISIM CV test and the OTE + ISIM (OTIS) test are shown in Figure 2.
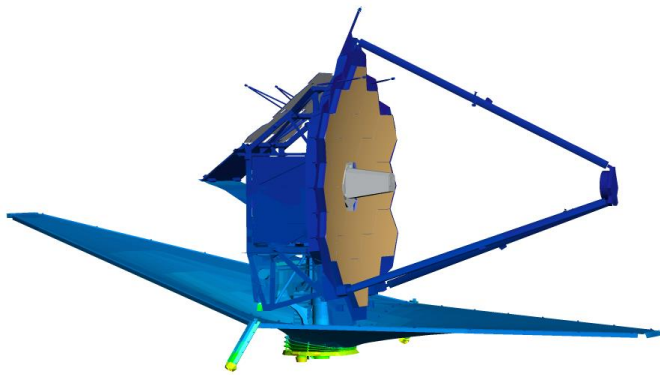

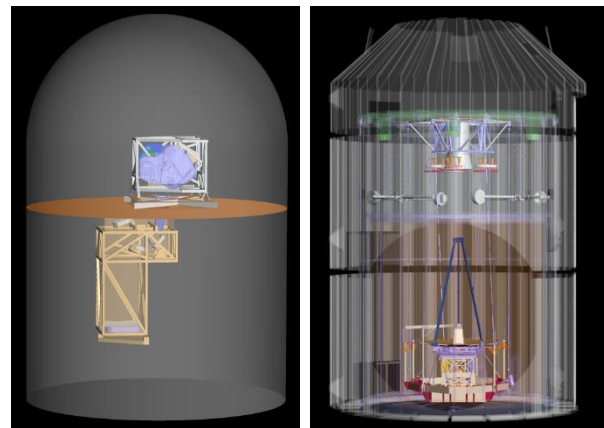Figure 1. Flight Observatory configuration

Figure 2. Configurations for OSIM + ISIM in the GSFC SES chamber (left); integrated OTE + ISIM, "OTIS" in JSC Chamber A (right).
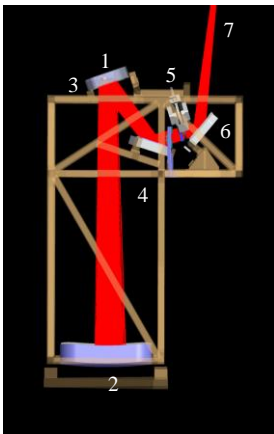

Figure 3. OSIM with a representative ray bundle.

In addition to the optical and mechanical elements in the model, an extensive series of scripts were written to automate the process of configuring and steering light sources, moving instrument mechanisms such as focus adjustment mirrors and pupil/filter wheels, providing configuration management of coatings, raytrace controls, importance sampling and scatter model assignments, and performing batch processing of multiple ray trace and analysis configurations. To date, the model has on the order of 120,000 elements, 185 light sources, 30 optical materials, 164 optical coatings, and 70 scatter functions.

Due to space constraints here, only the OSIM, NIRISS, and NIRCam subassemblies of the FRED model are described in detail. Instrument-level reports describing each of the other Science Instruments[1,2,3], and an overview of the Flight Observatory[4] can be found elsewhere.

2.1   OSIM

In order to test the ISIM Science Instruments after integration into the ISIM Structure, an Optical Telescope Element Simulator[5] (OSIM) was designed and built by Ball Aerospace to

provide a steerable, tunable light source that mimics the optical design of the OTE. Figure 3 shows the OSIM subassembly, with a representative ray bundle. Light is emitted from point sources from a Source Plate Assembly (1) located in a recessed back of Fold Mirror 1 (FM1). Light comes through one of a variety of holes in FM1 to the large spherical Primary Mirror (2), reflects back towards FM1 (3), to Fold Mirror 2 (4), through a dual wheel Pupil Select Mechanism (5), and off of a steerable Fold Mirror 3 (6), toward the ISIM Science Instruments (7). The Source Plate Assembly can move along and normal to the beam path providing control over focus and short-range steering in field space. FM3 is on a gimbal mount that provides field space steering over the entire ISIM field-of-view. Multiple light sources within the Source Plate Assembly provide monochromatic (laser diode), quasi-monochromatic (LED) and broad band (tungsten filament) sources appropriate to the SI of interest. A module of the Python steering code used to control the actual OSIM hardware was configured to be called from the FRED automation scripts and allow the OSIM model to be steered to the exact same configuration as the hardware.[6]
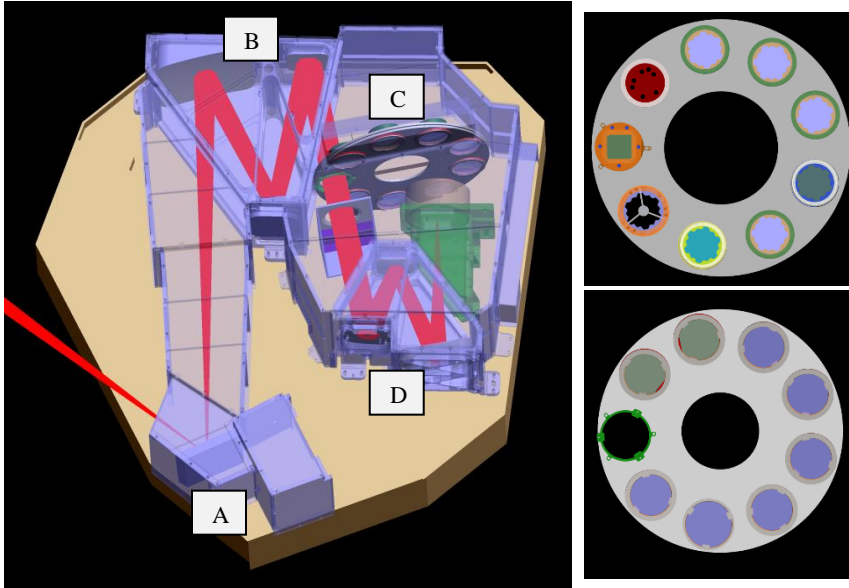

Figure 4. NIRISS instrument and optical path (left). Pupil wheel (upper right). Filter wheel (lower right).

2.2 NIRISS

The NIRISS instrument model and center field point optical path are shown in Figure 4. Light from the OTE, OSIM (for ISIM CV), or the AOS Source Plate Assembly (ASPA) in the OTIS test is incident from the left, and captured by a pick-off mirror (A), which also acts as a focus adjustment mechanism. Light then passes through (B) the Collimator three-mirror anastigmat (TMA), (C) the Dual Wheel (pupil wheel and filter wheel combination), a stray light baffle, and (D) the Camera TMA before reaching the detector. For a variety of functional, budgetary, and schedule reasons, NIRISS was not optically tested end-to-end in its final configuration prior to delivery to GSFC. While the optical path of the pick-off mirror, Collimator TMA, Camera TMA and focal plane was integrated and

aligned, the Dual Wheel was not included in those tests since it was being prepared in parallel as part of a rapid redesign after components of the initial Tunable Filter Instrument design failed to meet requirements. Therefore, there was no opportunity to experimentally assess stray light paths in the fully integrated instrument prior to the ISIM CV campaign. For these reasons, more effort was put into the construction and exercise of the NIRISS models than the other instruments prior to the ISIM CV tests.

Shown in the top right corner of Figure 4, the filter elements in the pupil wheel each contain a pupil stop mask that is slightly oversized compared to the imaged OTE pupil so as to block stray light from outside of the OTE pupil, but not vignette rays from the nominal optical path. The three other elements in the pupil wheel are the GR700XD cross-dispersed grism, the Non-Redundant Mask (NRM), and the Pupil Alignment Reference (PAR). The PAR is used in combination with long wavelength filters in the filter wheel in imaging mode. The NRM is used to perform aperture masking
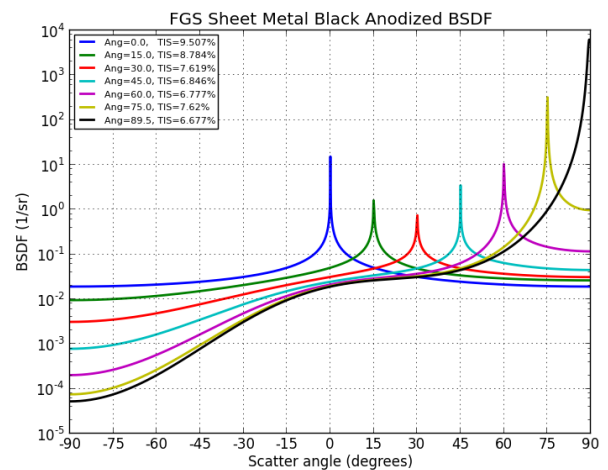

Figure 5. Example BRDF function created by fitting data delivered in the FGS End Item Data Package.

interferometry. The GR700XD grism performs Single Object Slitless Spectroscopy and is designed to disperse 0.9 to 2.8 um light in 1st order across the entire detector length. Since the grism material is ZnSe and there are no bandpass coatings applied to it, it will also pass other wavelengths that the detector is sensitive to (0.6-5 um) through the 0th order path and disperse wavelengths longer than 2.8 um, albeit at lower efficiency, that result in undesirable stray light paths.

Scatter models (functional representations of measured scattering profiles) for each coating in each instrument were generated by digitizing the scattering profiles provided in the delivered instrument End Item Data Packages and fitting those curves to appropriate functional representations. An example of one of the FGS/NIRISS Bi-Directional Reflectance Distribution Functions (BRDF) is shown in Figure 5.
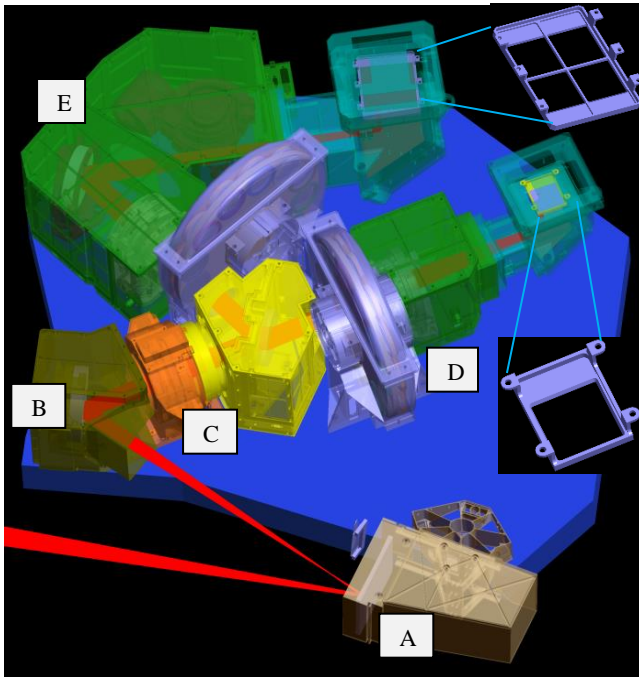

Figure 6. Module A of the NIRCam instrument, with extracted views of the hardware masks that sit immediately in front of the Focal Plane Array detectors.

2.3   Near Infrared Camera (NIRCam)

The NIRCam instrument model and a representative optical path are shown in Figure 6. Light from the OTE, OSIM, or ASPA is incident from the left, is captured by the Focus Adjustment Mechanism (FAM) (A), reflects off the First Fold Mirror, (B), and passes through the Collimator lens assembly (C). Wavelengths longer than 2.35 um pass through the Dichroic Beam Splitter (DBS), a Pupil/Filter Wheel assembly and a Camera lens assembly (D), and reflect off of a fold mirror before reaching the Long Wavelength (LW) Focal Plane Array (FPA) detector. Wavelengths shorter than 2.35 um reflect off of the DBS, pass through a Pupil/Filter Wheel assembly and Camera lens assembly (E), and reflect off of two fold mirrors before reaching the Short Wavelength (SW) FPA detectors. Shown in an exploded view, there are masks immediately in front of the detectors that shield hardware outside of the active detector pixels from direct illumination, reducing glints and back-reflections. The SW channel uses four 2048x2048 pixel H2RG detectors to cover the 2.2 arcminute field-of-view. The cross in the middle of the SW FPA mask covers the narrow gaps between the four detectors. The LW channel uses a single 2048x2048 detector for the same field.

It is important to note that there are two NIRCam Modules, A and B, that are identical, mirror images of each other on opposite sides of the optical bench. The implementation of the two Modules in the FRED model are somewhat different: Module A makes extensive use of the Faceted Surface element in FRED that approximates complicated structures with a collection of triangular surfaces tessellated together to cover an entire object. Such elements can more easily yield a high-fidelity hardware model, but have some limitations due to the uncertainty in determining their surface normal directions for the sake of calculating reflection/transmission angles, especially in the case of coherent beam propagation. Module B primarily uses the more conventional surfaces available in FRED. The combination of the two allows us to use whichever model is more appropriate to the analysis task at hand for cases that are not specific to the handedness or physical location of the Module.

3.   STRAY LIGHT CASES

While the model has been used for a wide variety of studies, three specific cases from the ISIM cryogenic vacuum test campaign (three tests referred to as "CV1RR", "CV2", and "CV3") demonstrate the value of combining the optical and high-fidelity mechanical designs in a non-sequential ray trace package to predict stray light features prior to testing and diagnose features found during testing. 1) The NIRISS Single Object Slitless Spectroscopy mode uses a cross-dispersed grism, the GR700XD, to disperse 0.9 to 2.8 um light across the length of the detector. The original optical design allowed for an unintended "skip path" where dispersed light exiting the grism bypasses two of the three focusing mirrors and results

in a broad background that contaminates the primary spectral trace. Other undesirable artifacts arose after a re-design that also required detailed investigation. 2) Ghost reflections observed in different NIRCam grism observations led us to determine that the orientation of filter elements in the NIRCam Module B flight hardware differs from that in the original optical model. This impacts the location of ghost artifacts and explains poorly understood aberrations in the NIRCam B weak lens modes observed in ISIM CV2 and CV3. 3) Scattering from the hardware baffles immediately in front of the NIRCam Focal Plane Assemblies can lead to contamination of science data if bright sources are located in a well-defined annular region around the fields-of-view.

3.1 NIRISS GR700XD

One of the NIRISS modes performs Single Object Slitless Spectroscopy (SOSS) of exoplanets transiting their local star using a cross-dispersed grism, the GR700XD. In its initial orientation, the grating surface of this element dispersed light in the plane of the Camera TMA, and the orientation of the three Camera TMA mirrors allowed for two undesirable light paths. The first, shown in Figure 7, is a path for 0th order light to reflect twice off of the 2nd and 3rd TMA mirrors each and reach the focal plane near the primary trace, but not directly overlap. The second, shown in Figure 8, is a path for dispersed light to directly reach the detector after reflecting from either the 1st or the 3rd TMA mirror, with the former path overlapping the primary trace. While the 0th order multi-bounce artifact is much brighter, it does not directly impact the primary trace. The second artifact, however, was predicted to be on the order of 3% of the peak signal in the primary trace, would cover more than half of the spectral length, and would result in a significant degradation in the performance of this mode.

Artifact specifics: Since the 0th order multiple-bounce path occurs at the very edges of each of the TMA2 and TMA3 mirrors, the location, morphology and intensity of this artifact is highly dependent on the precise size and location of the physical apertures of the TMA2 and TMA3 mirrors. The 1st order artifact overlapping the spectral trace consists of ~2.8-5.0 um light from the grism 1st-order *and* 1.4-2.5 um light from grism 2nd-order, meaning filtering out wavelengths longer than 2.8 um would not be an effective mitigation strategy
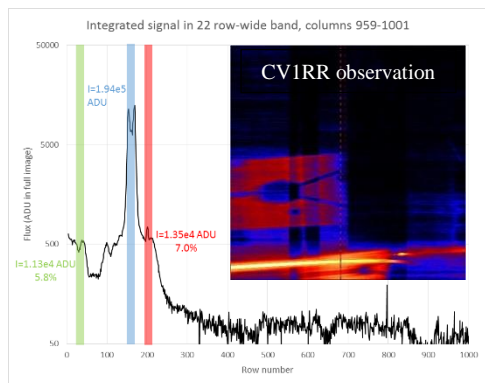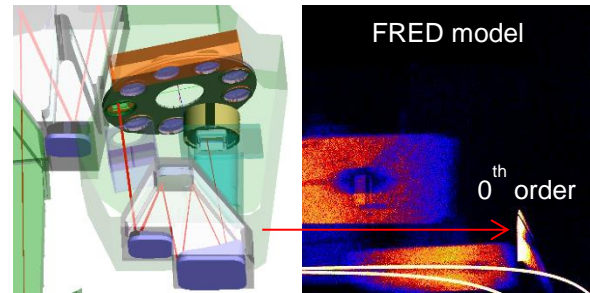

Figure 7. (left) Multi-reflection path of 0th order light. (right) Simulation of the GR700XD mode with 100M rays and a constant spectral content from 0.5 to 5.0 um. While this artifact was bright, it was not expected to directly impact the spectroscopic traces.
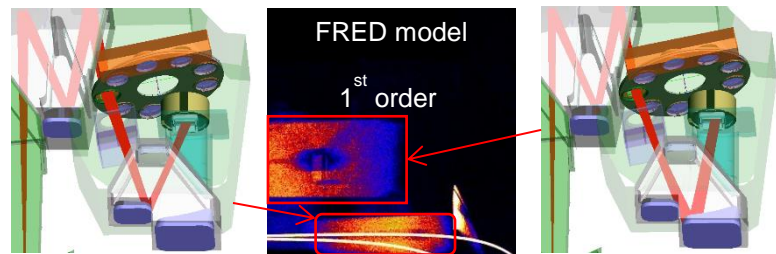

Figure 8. (left and right) "Skip paths" that allowed 1st order light to reach the detector after a single reflection from TMA1 or TMA3. (center) Simulation of the GR700XD mode. The path in the left-hand picture (grism-TMA1-detector) overlaps the spectral traces.

Figure 9. CV1RR observation of the grism mode, showing the predicted 0th and 1st order stray light artifacts.

These basic findings were confirmed when the CODE V optical model was modified to consider these paths, and observations in the ISIM Cryogenic Vacuum #1 Risk Reduction (CV1RR) test, shown in Figure 9, yielded remarkably similar behavior to the model results. While the model predicted a stray light contribution in the spectral trace of 3%, the ray trace was performed with a uniform spectral content, compared to the CV1RR observation that was taken with a blackbody light source and yielded 5-7% contamination depending on background subtraction specifics. Once the experimental result validated the models, the only mitigation that was found that would not potentially vignette other modes was to rotate the grism in the pupil wheel by 90-degrees. Modeling investigations done prior to CV1RR indicated that a 180-degree rotation would still yield some 1st order ghosting coincident with the long wavelength region of the primary trace, and an even stronger 0th order artifact that could impinge directly on the primary trace. Rotating 90-degrees in either direction would eliminate

the overlapping 1st order ghost and not result in other artifacts. (As a risk reduction prior to CV1RR, the NIRISS team had already begun design and fabrication of grism mounts that would allow for either 90-degree rotation.) The +90-degree orientation was selected for flight and a new grism with better efficiency was installed between CV2 and CV3 when the instruments were de-integrated from the ISIM structure to install new detector assemblies.

CV3 Orientation:

After installation of the new grism in its +90-degree orientation, observations during CV3 included a relatively dim artifact near the center of the spectral trace, shown in Figure 10. The peak intensity is approximately 1% of the peak in the spectral trace, and the tail of the artifact that overlapped the spectral trace is less than 0.1% of the trace peak. Unfortunately, the location of the trace changes as a function of pupil wheel rotation angle, and so the spectral trace orientation could not be completely optimized to minimize the width of a vertical subarray without the artifact moving toward the spectral trace and becoming a significant contaminating factor. While the science in this new orientation is not expected to suffer from this artifact, the question remained about its origin, since modeling of the original orientation was so accurate and no artifacts were predicted for the new orientation.
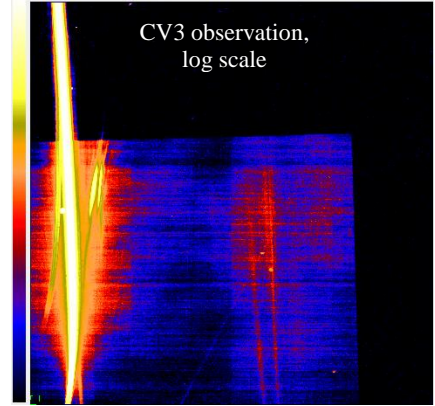

Figure 10. CV3 observation of an artifact near the 1st order trace.

The offending surface in this case is the inside edge of an aperture in the structural wall between the TMA2 and TMA3 mirrors of the Camera TMA housing. In Figure 11, the Camera TMA housing is isolated and shown without the TMA1 and TMA3 mirrors for clarity. 0th order light from the grism in red is refracted down towards the bottom of TMA1, reflects from TMA1 and TMA2, continuing slightly downward, where it grazes off the horizontal "window sill" surface immediately below TMA2 and (in yellow) is diverted back towards the detector field. In order to model this artifact, the raytrace analysis needed to be run in a coherent propagation mode that captured the mirror-like (specular) behavior of the surface at grazing incidence. The right hand of Figure 11 shows a combined incoherent and coherent ray trace. The incoherent rays produce the spectral traces, while the coherent rays produce the other artifacts shown. The observed and simulated images are overlaid in Figure 12, showing excellent agreement between the model and observation.
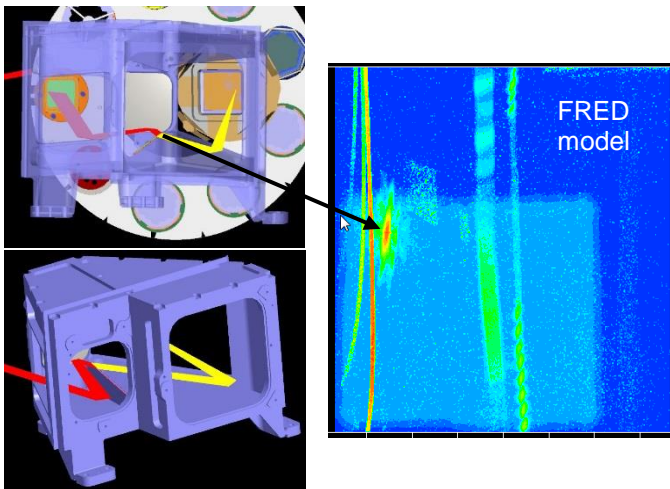

Figure 11. (left) "Window sill" surface causing the stray light artifact shown in associated ray trace (right).
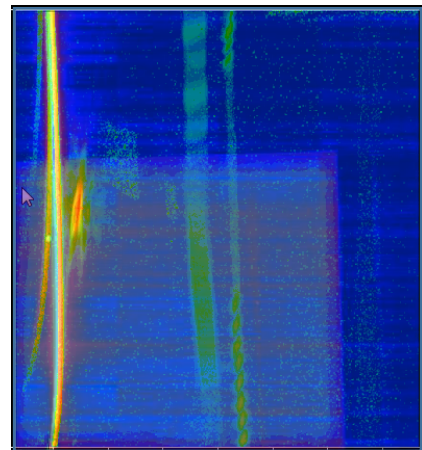

Figure 12. Observed and modeled grism images from Figure 10 and Figure 11 overlaid, demonstrating accurate correlation

Three primary factors contributed to the lack of understanding of artifacts in the new orientation:

1) The pre-CV1RR model of the Camera TMA housing did not include all surfaces in the hardware. Only one vertical wall (with the window cut-out) between the two regions of the housing was included, not the thin horizontal surface that causes this artifact. The model of the housing was later replaced using higher-fidelity Faceted Surfaces. However,

as noted in Section 2.3, this type of surface does not propagate reflected coherent diffraction properly due to the variable nature of the surface normals of each facet. In order to replicate the observed artifact, a standard FRED plane was created just above the window sill Faceted Surface.

2) The scattering parameters applied to the window-sill surface result in scattered light being spread uniformly across the field and give the appearance of broad, diffuse scatter. For either the Faceted Surface or the standard FRED plane, allowing only the specularly reflected ray, and assigning parentage to the reflected ray no matter the reflectance value, causes the artifact to be focused to a spot at the center of the observed artifact. Since we did not expect the scattering behavior of the model to so dramatically differ from reality, we did not investigate the behavior of the model for purely specular conditions after the faceted surface representation of the Camera TMA was implemented.

3) The vertical length of the artifact is due to coherent diffraction, not simple incoherent scattering. Because of the inability of faceted surfaces to propagate reflected diffraction, it was not until the more standard FRED plane was included *and* assigned a specularly reflecting function *and* a coherent light source was used did the full artifact morphology emerge.

In summary, the non-sequential nature of the stray light model allowed for rapid identification of the original ghost artifact in the pre-CV1RR configuration, but only the combination of a non-sequential model, a high fidelity hardware model and appropriate surface property assignments allowed for insight into the source of CV3 artifact. Mitigation strategies to move the artifact out of the field of interest exist, but they come at the cost of unacceptable losses in science data.

3.2 NIRCam filter orientation

The NIRCam long wavelength pupil wheels (part of "D" in Figure 6) each contain a variety of optical elements, including bandpass filters, coronagraphic Lyot stops, and grisms. They are followed by a filter wheel, where the filter elements are tilted 4-degrees with respect to the optical axis in order to direct any ghost reflections between pupil and filter wheel elements away from the optical path so that they do not reach the detector. The two grisms in each pupil wheel, GRISMR and GRISMC, disperse light along the rows and columns of the NIRCam detectors, respectively, with the length of the dispersed trace at the detector limited by the choice of filter wheel element. NIRCam Module A GRISMR observations during the CV2 test campaign showed a focused artifact at a constant offset from the targeted field angle, an example of which is shown in Figure 13. This was not originally expected because the path only occurs (as shown in Figure 14) for light that transmits through the grism in 1st order (red), reflects backward from the filter element (green), *and reflects forward again in 1st order* (blue) from the grating surface. (Only the
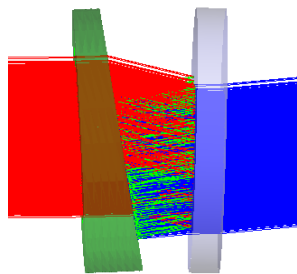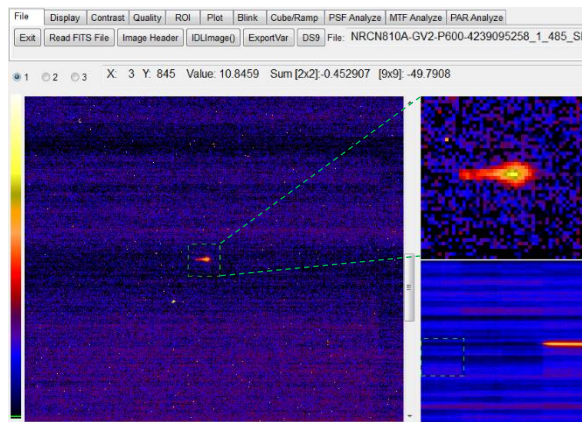
CV2 observation

Figure 13. CV2 observation of a focused artifact in a GRISMR image that tracks the field angle of the light source. The bottom right shows the full field image. The left window is an intermediate subarray, and the top right is a highly zoomed region around the artifact.
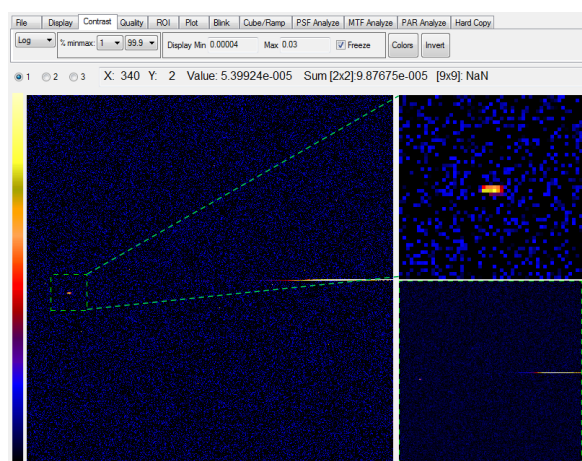
FRED model

Figure 15. Model result demonstrating a correlation to a reflection ghost path between the GRISMR element and the filter wheel element.

Figure 14. Ghost path between the GRISMR (green) and filter element (grey).

combination of 1st-order transmission and 1st-order reflection yields a quasi-focused spot at the detector. Combinations of 0th and 1st order yield dispersed light that is below the sensitivity of the detectors normal exposures.) The primary trace and artifact from this path are shown in a simulated image in Figure 15.
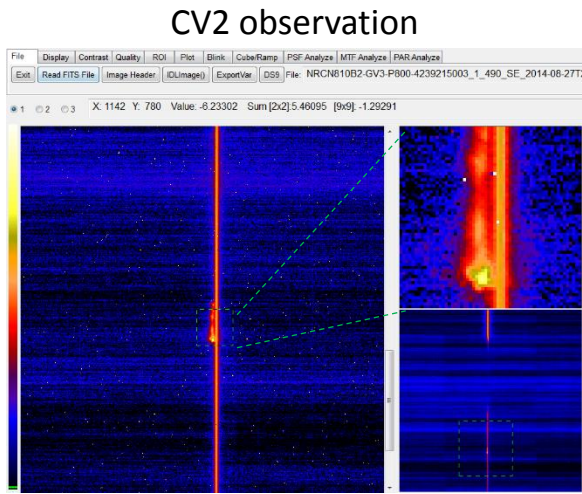
CV2 observation

Figure 16. Focused artifact in a Module B GRISMC image, similar to that seen in the Module A GRISMR observation in Figure 13.
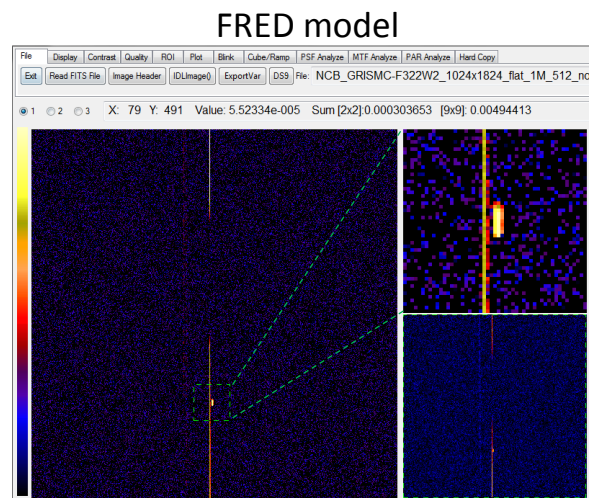
FRED model

Figure 17. Model result demonstrating a correlation to a reflection ghost path between the Module B GRISMC and the filter wheel element.

Images taken with the GRISMR in Module B do not show any such artifacts, but images with GRISMC (Figure 16) do show similar behavior. This was unexpected, since the two modules have mirrored, but otherwise identical optical models, so the artifact seen in Module A GRISMR should also be seen in Module B GRISMR. The artifact could only be reproduced in the FRED model by tilting the filter element far from its optical design position, and the resulting orientation of the filter element significantly violated the bounds of the filter mount from the original CAD model. The modeled artifact is shown in Figure 17. A graphical comparison of the CODE V and FRED filter tilts is shown in the left of Figure 18. The perturbed FRED element is in grey and the 2nd surface of the CODE V filter is in translucent green. Inspection of the as-built drawings of the Module B filter wheel showed that the B wheels are not mirrored versions of the Module A wheels as the optical model would dictate, but are identical to the Module A wheels. A corrected, non-mirrored model of
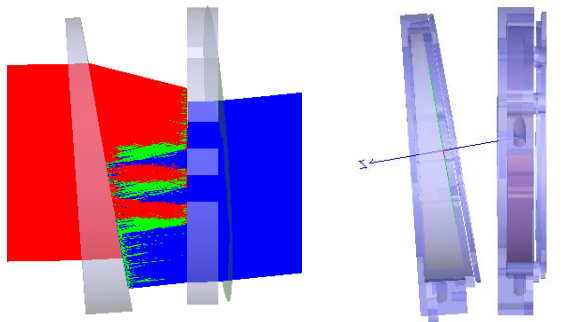

Figure 18. (left) Optical path leading to the Module B GRISMC artifact. The nominal Code V filter surface is also shown in translucent green, tilted with respect to the FRED filter element. (right) FRED optical and corrected hardware elements re-imported from CAD, showing that the FRED filter orientation fits in the CAD model, but the Code V filter element would not.

the hardware was imported into the FRED model and the FRED filter element then fit perfectly in its mount, confirming the disagreement between the CODE V and CAD models. The optical result is that the 4-degree tilt of the filter elements in Module B is clocked 90-degrees around the optical axis. (This change is being incorporated for future optical model deliveries.) One upside to this discrepancy is that the Module A GRISMC and Module B GRISMR modes do not have such ghost artifacts, so grism observations can be done in both orientations (albeit with different NIRCam Modules) without the ghost artifact occurring in either. Another impact of this work is the realization that the long wavelength filter tilts also apply to the short wavelength filter wheel. One element in the short wavelength filter wheel is a weak lens that nominally has a compensating mount to re-orient the lens normal to the optical axis. But because of the filter wheel geometry in Module B, the compensation is in the wrong axis, and this lens is still tilted with respect to the optical axis, introducing a significant coma term to images taken with this

element. Understanding this tilt and incorporating the expected aberration allows the wavefront sensing software to operate properly despite the misalignment.
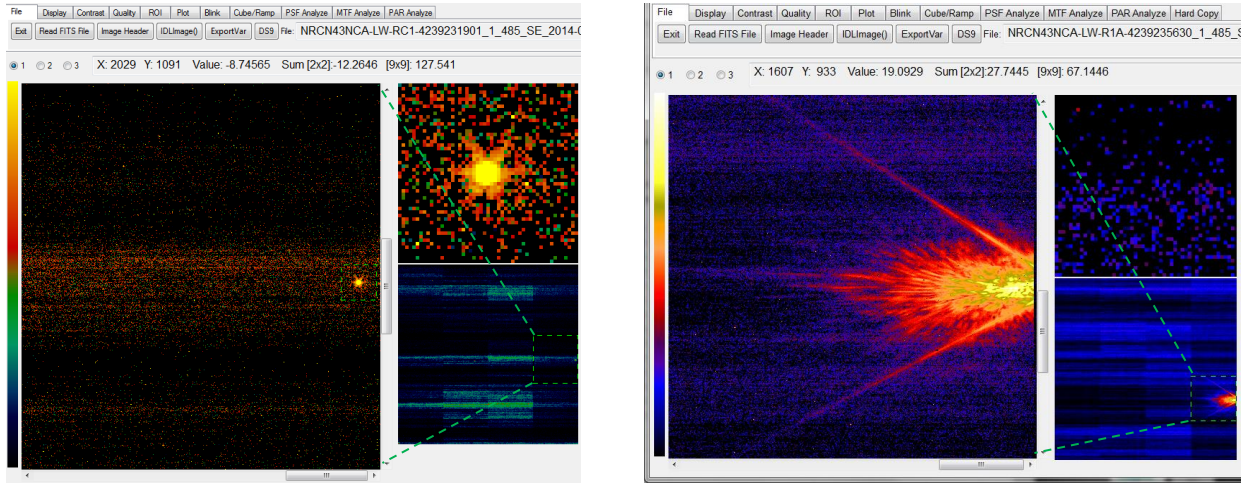

Figure 19. (left) Example of an in-field PSF near the edge of the field-of-view in the long wavelength channel of NIRCam Module A. (right) Example of light scattering into the field when the light source is pointed approximately 2 arcseconds outside the field-of-view. Note: The light source in the right figure is 30x brighter than that in the left figure.

3.3 NIRCam "dragon's breath" scattering

Tests in ISIM CV2 showed that when a bright point source is located just outside of the field-of-view of either of the NIRCam LW channels, a burst of scattered light is observed for a small range of field angles. Figure 19 shows examples of a normal, broad band, in-field point source in the LW channel of NIRCam Module A. Scattered light is observed when the point source is observed 2.56 arcseconds outside of the field-of-view. (The out-of-field image was taken with the light source at 30 times brighter than the in-field image to draw out any stray light effects.) Including the diffraction spikes from the tricontagon-shaped pupil (the strong lines at 8 o'clock and 10 o'clock), the total amount of light reaching the detector in the scattered image is 3.3% of incident light, though the peak pixel in the scattered light region is 0.09% of the peak in an equivalent in-field observation. Thus, if a bright object is located ~2.5 arcseconds from the field edge during a science observation, the local portion of the image near that point m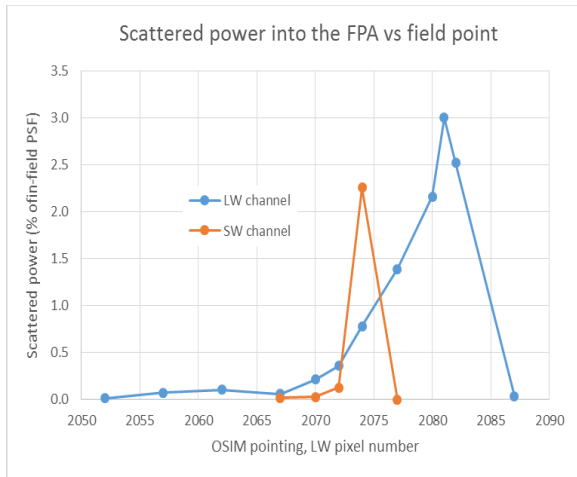ay be contaminated with stray light. Relatively speaking, this effect is small, but while no science requirements are violated, it is an artifact of interest for observers to be aware of.
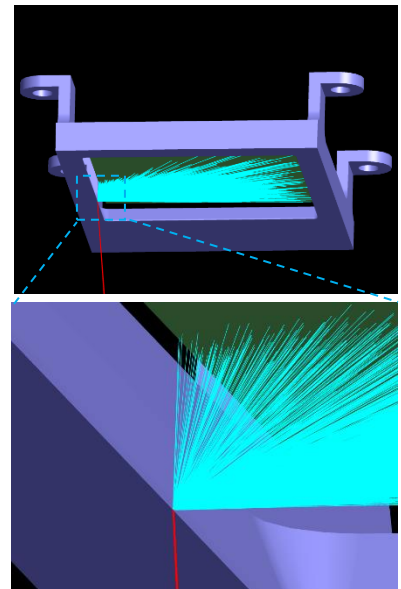

Figure 20. (top) Out of field rays (red) scattering off of the shallow knife edge wall of the NIRCam A long wavelength FPA mask and into the field of view (cyan). (bottom) Magnified view of the region where scattering occurs.

Figure 21. Total power scattered into the field-of-view vs field point in virtual pixels in the long wave channel.

The mechanism for this scattering was not initially well understood, so modeling was performed to correlate the scattering behavior and predict the field angles over which this effect occurs. Shown in Figure 6, the NIRCam FPAs each have a hardware mask covering the region just in front of and outside of the active FPA pixels from direct illumination. The inner edges of these masks have a shallow edge parallel to the optical path that can scatter

out-of-field light at grazing angles back into the field-of view. A view of the NIRCam A LW FPA mask is shown in Figure 20. The top half of the figure shows the narrow fraction of the whole beam bundle incident from underneath the hardware mask (red). A magnified view is shown in the bottom half of the figure, showing where incident light is scattered back into the field (cyan). A series of ray traces were performed for point sources starting from the edge of the field of view out to ~3 arcseconds beyond the edge of the field. (Configuration of the OSIM light source in the model can be specified in sky angle or in terms of pixel positions. It is simpler to perform a scan normal to the direction of the edge of the field-of-view using virtual pixels, so the scan was done from the edge of the field (pixel 2047) to 40 pixels beyond the edge (pixel 2087) in 5-pixel increments.) The results are shown in Figure 21 for both the LW and SW channels. Observational data was not collected in the SW channel in ISIM CV2, but the SW FPA mask has similar geometry to that in the LW channel, so similar scattering is to be expected. One can see that the range of the modeled effect in the SW channel is less than ±2 pixels, significantly narrower than the ±8 pixels in the LW channel, but the peak scattered power is on the same order as the LW.

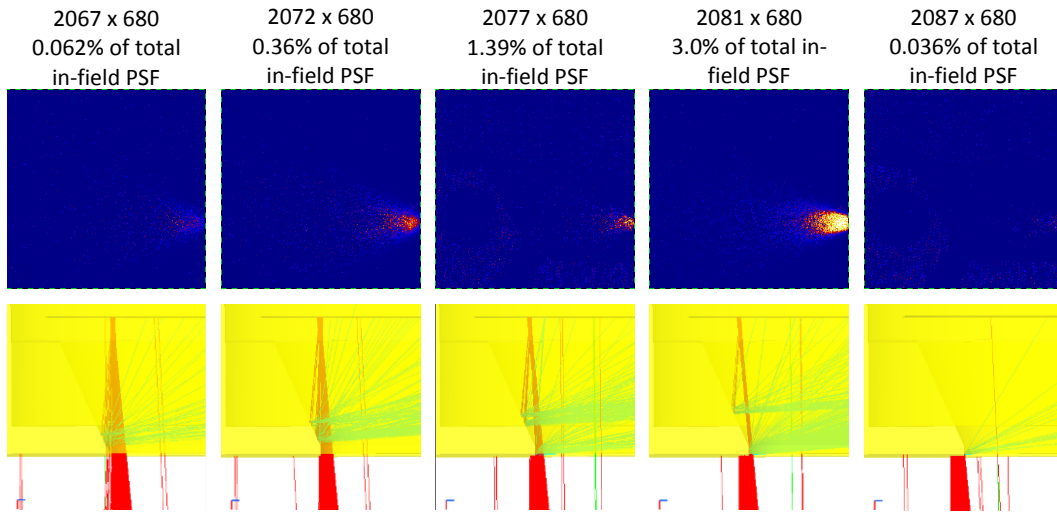| 2067 x 680 0.062% of total in-field PSF | 2072 x 680 0.36% of total in-field PSF | 2077 x 680 1.39% of total in-field PSF | 2081 x 680 3.0% of total in-field PSF | 2087 x 680 0.036% of total in-field PSF |

Figure 22. (top row) Modeled scattering distribution over LW channel field-of-view. (bottom row) Cross-sectional view of the LW FPA mask (yellow) with rays incident from below (red) and scattering from the mask (green), as well as reflecting from the FPA surface and scattering from the back of the FPA mask.

The scattering distribution and a cross-sectional view of the LW channel FPA mask with rays traced are shown for selected field points in Figure 22. There are actually two paths that lead to scattered light (direct scattering from the FPA mask, and light reflected from the FPA surface and scattered from the back beveled surface of the FPA mask). The direct path
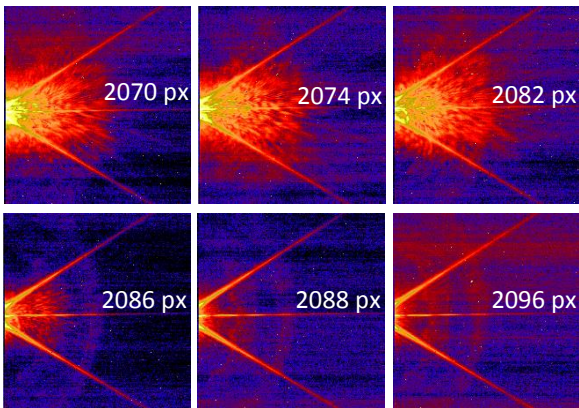

Figure 23. Selected data from the ISIM CV3 out-of-field scan in the LW channel. The total power increases as the source is scanned from pixel 2070 to 2082, then falls off rapidly.
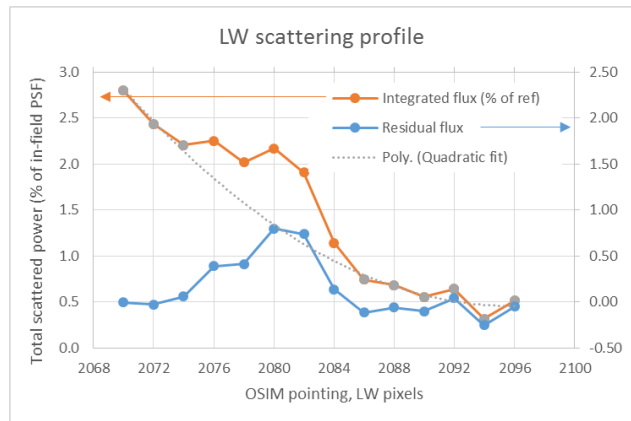

Figure 24. (orange) Plot of the total scattered power vs source field position in virtual LW pixels. (blue) Residual power after subtracting a quadratic fit to the points in grey in the raw data.

(incident light scattering from the FPA knife edge) is the dominant source as the path is at grazing angles where even diffuse, "black" surfaces tend to be highly reflective.

Based on this modeling, a similar scan was implemented during the ISIM CV3 test from 22 to 48 LW pixels out-of-field (pixel 2070 to 2096) in 2-pixel increments, taking data in both the short and long wavelength channels. Selected images from the LW channel scan are shown Figure 23, showing that some scattering already occurs at a field point of 2070 pixels, the furthest in-field point sampled, and continues to pixel 2082, beyond which scattering falls off rapidly.

A plot of the total in-field power at each field point is shown in Figure 24 in orange. A quadratic fit to the innermost and outermost points is subtracted off to estimate the range over which significant scattering occurs, shown in blue. Since scattering occurs at the innermost field point tested, this subtraction most likely underestimates the width of the scattering range somewhat. One change between CV2 and CV3 that affects the magnitude and location of the scattering region is that the FPA masks were replaced with new flight hardware that had tighter fabrication tolerances and were co-aligned to the active pixel region of each FPA more accurately. These changes resulted in a more consistent location and range for the scattering region outside of each field-of-view edge, and an improved dark coating reduced the total scattered power by a factor of 3 compared to the CV2 result.
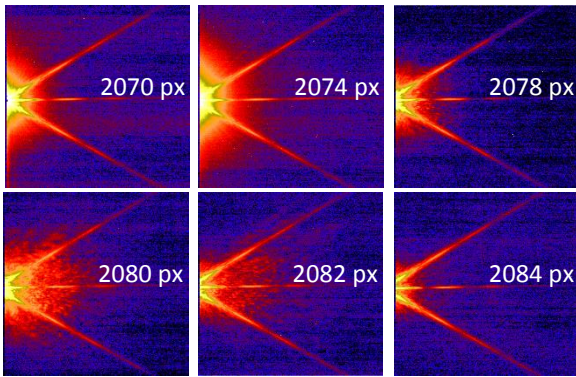

Figure 25. Selected data from the ISIM CV3 out-of-field scan in the SW channel. The scattering region is clearly limited to a ±2-3 pixel range around 2080 pixels.
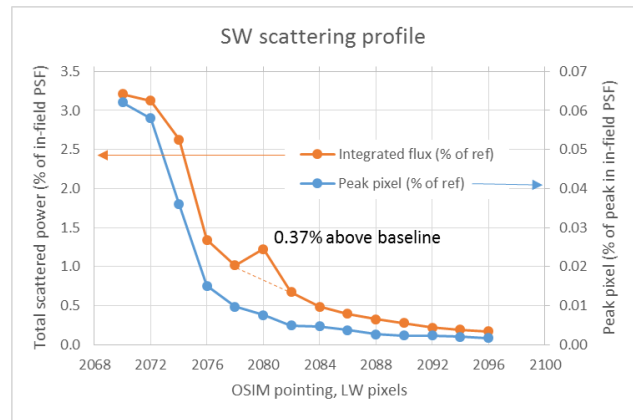

Figure 26. (orange) Plot of the total scattered power vs source field position in the SW channel as a function of pointing in virtual LW pixels. (blue) Peak pixel in the scattering region as a percentage of the peak in an equivalent in-field PSF.

Figure 25 and Figure 26 show similar data for the SW channel. The region over which scattering occurs is extremely narrow - ±2-3 LW pixels, or ±0.2 arcseconds. Also, since the diffraction effects from the primary PSF are more clearly visible outside the scattering region, their contribution can more reliably subtracted off, yielding an estimate for the worst case scattering into the field of <0.4% of the total power in the incident beam bundle. The peak pixel in the scattering region is similarly small at approximately 0.01% of the peak in an equivalent in-field PSF.

In summary, a combination of observation and modeling demonstrates that there is a narrow region outside of each field-of-view edge in NIRCam where scattering can occur from the mask immediately above the FPA and reach the active pixels. In the LW channels, this range is estimated to be centered at 32 LW pixels (2.05 arcseconds) from each edge of the field-of-view, and be ±6 pixels (±0.4 arcseconds) wide at a minimum and probably closer to ±10 pixels (±0.65 arcseconds) wide. The peak in the total scattered power curve estimates that 1% of the incident light will be scattered into the science field. In the SW channels, the effect is clearly narrower and less intense, with a ±3 pixels (±0.2 arcseconds) width centered at 30 LW pixels (2.0 arcseconds) from each edge of the SW field-of view. Less than 0.4% of the incident light is scattered into the field, and the peak pixel in the scattering region is less than 0.01% of the peak in an equivalent in-field PSF. It should be noted that this effect does not violate any science requirements associated with NIRCam, but will be documented as an advisory to observers to avoid pointing configurations that place bright objects in these regions around the fields-of-view.

4. CONCLUSIONS

A complete, fully integrated stray light model of the James Webb Space Telescope was constructed in the FRED Optical Engineering Software package, from original CAD models, thermal models, and material property data from a wide variety of sources. There are multiple, selectable configurations available including the flight Observatory, the ISIM CV test campaign, and the upcoming OTIS test at JSC. The three stray light cases presented here, encountered during the ISIM CV campaign, were predicted and/or diagnosed using the model, with model results matching the observations unambiguously. In all three cases, the combination of non-sequential ray tracing and a high-fidelity hardware model were necessary to properly diagnose observed artifacts. Beyond that, diagnosis of one of the cases, the NIRCam grism artifacts, uncovered an error in the mechanical design that put optical elements in an orientation at odds with the optical model.

The stray light model continues to be updated and expanded. Other topics that have been investigated include detection of thermal self-emission of the flight Observatory in each Science Instrument, OTE pupil imaging using the Beam Image Analyzer during the "OGSE2" test at JSC, cross-checks of coherent PSF morphology for the OGSE2 and OTIS tests, and ghost artifacts in the NIRISS instrument in imaging and wide-field slitless spectroscopy modes.

5. ACKNOWLEDGEMENTS

6. REFERENCES

[1] Doyon, R. *et al.*, "The JWST Fine Guidance Sensor (FGS) and Near-Infrared Imager and Slitless Spectrograph (NIRISS)," Proc. SPIE 8442, (2012)

[2] Wright, G. S., *et al.*, "Design and development of MIRI, the mid-IR instrument for JWST," Proc. SPIE 7010, (2008)

[3] Bagnascoa, G. *et al.*, "Overview of the Near Infrared Spectrograph (NIRSpec) Instrument on-board the James Webb Space Telescope (JWST)," Proc. SPIE 6692, (2007)

[4] Greenhouse, M. A., "The JWST Science Instrument Payload: Mission Context and Status," Proc. SPIE 9602, (2015)

[5] Sullivan, J. F., *et al.*, " JWST's optical telescope simulator for verification of the Integrated Science Instrument Module," Proc. SPIE 9951, (2016)

[6] Sabatke, D., *et al.*, "Ray-tracing for coordinate knowledge in the JWST Integrated Science Instrument Module," Proc. SPIE 9293, (2014)